Journal of Materiomics 10 (2024) 1026–1035

Contents lists available at ScienceDirect

Journal of Materiomics

journal homepage: www.journals.elsevier.com/journal-of-materiomics/

Research paper

High energy storage density in $NaNbO_3$ antiferroelectrics with double hysteresis loop

Li Ma [a, b, 1], Zhenpei Chen [a, 1], Gengguang Luo [a, 1], Zhiyi Che [a], Chao Xu [c], Dongliang Shan [d], Zhenyong Cen [a], Qin Feng [a], Xiyong Chen [a], Toyohisa Fujita [a], Ye Zhu [c], Yunya Liu [d], Jing-Feng Li [e, **], Shujun Zhang [f, ***], Nengneng Luo [a, *]

[a] State Key Laboratory of Featured Metal Materials and Life-cycle Safety for Composite Structures, School of Resources, Environment and Materials, Guangxi University, Nanning, 530004, China
[b] School of Chemistry and Chemical Engineering, Guangxi University, Nanning, 530004, China
[c] Department of Applied Physics, Research Institute for Smart Energy, The Hong Kong Polytechnic University, Hung Hom, Kowloon, Hong Kong, China
[d] Key Laboratory of Low Dimensional Materials and Application Technology of Ministry of Education, School of Materials Science and Engineering, Xiangtan University, Xiangtan, 411105, Hunan, China
[e] State Key Laboratory of New Ceramics and Fine Processing, School of Materials Science and Engineering, Tsinghua University, Beijing, 100084, China
[f] Institute for Superconducting and Electronic Materials, Australian Institute of Innovative Materials, University of Wollongong, Wollongong, NSW, 2500, Australia

ARTICLE INFO

Article history:
Received 10 October 2023
Received in revised form
3 November 2023
Accepted 10 November 2023
Available online 29 November 2023

Keywords:
Sodium niobate
Antiferroelectrics
Double hysteresis loop
Energy storage performance
Reversibility

ABSTRACT

Antiferroelectrics (AFEs) possess great potential for high performance dielectric capacitors, due to their distinct double hysteresis loop with high maximum polarization and low remnant polarization. However, the well-known $NaNbO_3$ lead-free antiferroelectric (AFE) ceramic usually exhibits square-like *P*–*E* loop related to the irreversible AFE P phase to ferroelectric (FE) Q phase transition, yielding low recoverable energy storage density (W_{rec}). Herein, significantly improved W_{rec} up to 3.3 J/cm^3 with good energy storage efficiency (η) of 42.4% was achieved in $Na_{0.7}Ag_{0.3}Nb_{0.7}Ta_{0.3}O_3$ (30Ag–30Ta) ceramic with well-defined double *P*–*E* loop, by tailoring the A-site electronegativity with Ag^+ and B-site polarizability with Ta^{5+}. The Transmission Electron Microscope, Piezoresponse Force Microscope and *in-situ* Raman spectra results verified a good reversibility between AFE P phase and high-field-induced FE Q phase. The improved stability of AFE P phase, being responsible for the double *P*–*E* loop and improved W_{rec}, was attributed to the decreased octahedral tilting angles and cation displacements. This mechanism was revealed by synchrotron X-ray diffraction and Scanning Transmission Electron microscope. This work provides a good paradigm for achieving double *P*–*E* loop and high energy storage density in $NaNbO_3$-based ceramics.

1. Introduction

As the core of high power and pulsed power systems, dielectric capacitors have been actively studied in the past decades due to their high power density, and fast charge-discharge capability [1–5]. The recoverable energy storage density (W_{rec}) of a dielectric capacitor can be evaluated by the integration between hysteresis loop and *y* axis, according to the equation: $W_{rec} = \int_{P_r}^{P_m} EdP$, where P_m and P_r are maximum and remnant polarizations under electric field (E), respectively [6–8]. This means large P_m and small P_r are the key requirements for achieving a high W_{rec}. Among numerous dielectric materials for energy storage application, the antiferroelectric (AFE) materials exhibit exceptional benefits compared to other dielectric categories, such as linear dielectric and ferroelectrics, due to the unique double polarization-electric field (*P*–*E*) loop with high P_m and low P_r [9]. Achieving double *P*–*E* loop with

* Corresponding author.
** Corresponding author.
*** Corresponding author.
E-mail addresses: jingfeng@mail.tsinghua.edu.cn (J.-F. Li), shujun@uow.edu.au (S. Zhang), nnluo@gxu.edu.cn (N. Luo).
Peer review under responsibility of The Chinese Ceramic Society.
[1] Authors contributed to this paper equally.

https://doi.org/10.1016/j.jmat.2023.11.003

smaller P_r and hysteresis as well as larger P_m is good for realizing higher W_{rec}. Particularly, the lead-free AFEs are considered as promising candidates under the demand for environment friendly development [10,11].

Over the past 70 years, there has been great interest in sodium niobate ($NaNbO_3$, NN) as a viable AFE material [12,13]. The pure NN ceramic usually exhibits multi-phases coexisting state at room temperature (T_R), in which the majority of AFE P phase (*Pbma* space group) mixes with minor FE Q phase ($P2_1ma$ space group), originating from their similar free energy [14,15]. The P phase transforms into Q phase easily under enough electric field, which preserves after field removal [14]. As a result, a square FE-like *P*–*E* loop with large hysteresis and high P_r is always observed in pure NN ceramic, leading to inferior W_{rec} of ~0.12 J/cm^3 [16]. In order to improve the W_{rec}, intensive investigations have been performed, mainly focusing on two strategies: (1) stabilizing the AFE P phase to obtain double hysteresis loop; (2) down-tuning the high temperature R phase (*Pnma* space group) around T_R to realize a relaxor state. The former aims to utilize both the high P_m, low P_r, and large AFE-FE phase transition electric field (E_{AF}) of an AFE material. Despite the development of a large number of NN-based AFE materials, the resulting materials typically exhibit a moderate W_{rec} of 0.55–1.70 J/cm^3 with low energy efficiency (η) of ~33% due to the pinched *P*–*E* loop associating with low E_{AF}, large hysteresis and high P_r [17,18]. The latter strategy of tuning to R phase is supposed to decrease P_r, reduce the hysteresis of *P*–*E* loop, and enhance the breakdown electric field, which can significantly improve the W_{rec} [19,20]. Nevertheless, no double *P*–*E* loop can be observed due to lack of AFE-FE phase transition. It appears that the ultrahigh electric field, rather than the unique AFE-FE phase transition, is responsible for both the large P_m and high W_{rec} in this case [21]. However, the lack of well-defined double *P*–*E* loop, generally observed in PZ ($PbZrO_3$)-based AFEs [22,23], is restricting the further improvement of energy storage density. Therefore, it remains crucial to develop NN-based ceramics with a well-defined double hysteresis loop for achieving high energy storage density.

Unfortunately, it is very hard to achieve typical double hysteresis loop in NN-based ceramics, despite many attempts have been carried out to stabilize the AFE P phase through decreasing the Goldschmidt tolerance factor (t) [16,24–26]. The decreased t signifies a reduction of the perovskite volume and the improvement of structure stability, which is conducive to enhance the AFE distortion [26,27]. Although the $CaTiO_3$, $CaZrO_3$, or $CaSnO_3$ with lower t compared to that of NN is modified to form solid solution, the low E_{AF}, large hysteresis, high P_r, and inferior W_{rec} are consistently obtained [17,25,28]. That is to say, simply decreasing t by tailoring the ionic radius is insufficient to achieve a well-defined double hysteresis loop. It is generally accepted that the inherent physical and chemical characteristics of both A- and B-site cations, in addition to the ionic radius, play a significant role in determining the perovskite volume and producing coupling effect between them, which will change lattice distortion and cation displacement, thereby influencing the stability of AFE phase [29–31]. Recently, well-define double hysteresis loop was achieved in $0.75NaNbO_3$-$0.2AgNbO_3$-$0.05CaHfO_3$ ceramic through decreasing t and electronegativity difference by co-doping both A- and B-site cations [32]. This shines a light on achieving double hysteresis loop and high W_{rec} in NN-based ceramics.

Herein, differing from the previous strategies [18,32], a new concept of simultaneously tailoring A-site electronegativity and B-site polarizability of NN is adopted to achieve well-defined double hysteresis loop and then improve the energy storage density without the decrease of t. In addition, according to previous studies on PZ-based AFEs, the reversibility of electric-field induced AFE to FE phase transition is the key feature for a double hysteresis loop [33]. To date, although several studies have been employed to investigate the electric-field induced AFE P to FE Q phase transition in NN-based ceramics, the rigorous understanding of the phase transition is still absent. Therefore, it is of particular importance to develop effective *in-situ* or *ex-situ* measuring techniques to evaluate the reversibility between AFE P and FE Q phases. In this work, a series of NN-based ceramics with compositions of $Na_{1-x}Ag_xNb_{1-y}Ta_yO_3$ (100*x*Ag-100*y*Ta) were developed by decreasing B-site polarizability and A-site electronegativity difference through A- and B-site co-doping method. As expected, well-defined double hysteresis loop together with substantially improved W_{rec} of 3.3 J/cm^3 and elevated η of 42.4% was achieved in 30Ag–30Ta. The *ex-situ* Piezoresponse Force Microscope (PFM) and Transmission Electron Microscope (TEM) measurements for the virgin and poled samples and *in-situ* electric field dependent Raman spectra were utilized to evaluate the reversibility of AFE P to FE Q phase transition. The underlying mechanism was revealed by the synchrotron X-ray diffraction (SXRD) and Scanning Transmission Electron microscope (STEM).

2. Experimental section

Fabrication of ceramics: $Na_{1-x}Ag_xNb_{1-y}Ta_yO_3$ (denoted as 100*x*Ag-100*y*Ta, $x = 0, 0.1, 0.2, 0.3, 0.4$; $y = 0, 0.1, 0.2, 0.3, 0.4$) ceramics were synthesized by a conventional solid-state reaction method, same to our previous work [34]. The Ag_2O (99.7%), Na_2CO_3 (99.8%) (Sinopharm Chemical Reagent Co., Ltd, China), and Nb_2O_5 (99.99%), Ta_2O_5 (99.99%) (Jiujiang tanbre Co., Ltd, China) were employed as raw materials. The raw materials were carefully weighed based on nominal composition and mixed in anhydrous ethanol using ball-milled for 10 h. Then, the mixtures were dried and calcined around 900 °C for 6 h in flowing O_2 atmosphere. Thereafter, the calcined powders were ball milled, dried again and hand-pressed into pellets, followed by the cold isostatic pressing at 250 MPa for 30 min to improve density of pellets. Afterwards, the green pellets were sintered at 1,280–1,400 °C, depending on the compositions, for 6 h in O_2 atmosphere. Finally, as-sintered pellets were polished down to ~100 μm and then coated with fire-on silver electrode of 2 mm in diameter on two parallel surfaces at 600 °C for 30 min to conduct normal electric measurements. Before several measurements related to poling state, the samples of NN, 0Ag–30Ta and 30Ag–30Ta were treated using DC electric fields under 140, 240 kV/cm and 330 kV/cm, respectively, which were obvious over their AFE-FE phase transition electric field.

Characterization of phase structure: Phase purity and crystal structures were characterized by using an X-ray powder diffraction (SmartLab-3kW, Rigaku Ltd., Tokyo, Japan) employing Cu K_α radiation under an acceleration condition of 40 kV and 40 mA, equipped with a temperature increasing part. The high-quality SXRD data were performed at TPS 09 A (Taiwan Photon Source) of the National Synchrotron Radiation Research Center with a calibrated wavelength of 0.826569 Å and the energy of 15 keV. The Rietveld analysis of the SXRD was performed using GSAS software. The TEM and selected area electron diffraction (SAED) were performed on a field-emission TEM (FE-TEM, JEM-2100F, JEOL, Japan) at an accelerating voltage of 200 kV. The *in-situ* Raman spectra were carried out using a laser confocal Raman microspectroscopy (LabRAM HR800, Horiba Jobin Yvon, France) on the surface of samples with excitation at 532 nm, connected with the withstand voltage tester (MS2671AN, Nanjing Minsheng Electronic Instrument Co., Ltd, China). Before this *in-situ* measurement, thin indium tin oxide (ITO) electrodes of 2 mm in diameter were sputtered onto two parallel surfaces of the ceramics, which disk thickness is ~80 μm. Aberration-corrected STEM was performed on a probe corrected FEI Spectra 300 S/TEM (ThermoFisher Scientific, Eindhoven,

Netherlands) equipped with an X-FEG source and operated at an accelerating voltage of 300 kV. A beam current of 50 pA and a semi-angle of convergence of 24.4 mrad (1 mrad = 0.0573°) was utilized. The annular dark field (ADF) image was collected with a detector semi-angle range of 72–200 mrad. Atom column locations were determined *via* 2D Gaussian fitting.

Characterization of topography: The microstructure was observed through a scanning electron microscope (FE-SEM Sigma 300, ZEISS Corp., German), after polished and thermally etched 30 min at temperature around 150 °C below the sintering temperature. The atomic force microscope (MFP-3D, Asylum Research, America) equipped with a PFM module was used to determine the PFM amplitude on the well-polished samples with the scanning AC voltage of 5 V.

Measurements of dielectric, impedance and piezoelectric properties: The dielectric permittivity and loss were measured using a precision impedance analyzer (E4990A, Keysight, Bayan, America) connecting with a temperature control system (DMS-2000, Balab, Wuhan, China) over the temperature ranging from −160 °C to 450 °C at 1, 10 kHz and 100 kHz. The piezoelectric coefficient d_{33} were measured using a Piezo-d_{33} m (ZJ-3A, Chinese Academic Society, Beijing, China). The electric field dependence of normalized dielectric permittivity was measured using a ferroelectric tester (TF Analyzer 3000, aixACCT, Aachen, Germany) with different bias field plus a small superimposed signal of 50 V at 1 kHz.

Measurements of ferroelectric properties and strain: The polarization *vs.* electric field hysteresis (*P*–*E*) loops, current *vs.* electric field (*I*–*E*) curves and strain *vs.* electric field (*S*–*E*) curves were characterized at 10 Hz using a ferroelectric tester, connected to a customized heating system. The discharge energy density and speed were measured using the capacitor charge-discharge test system (PKCPR1701, PolyK Technologies, PA, USA).

3. Results and discussion

Fig. 1a–c displays the *P*–*E* loops for the three representative compositions of NN, 0Ag–30Ta, and 30Ag–30Ta ceramics, respectively. A square-like hysteresis loop with high P_r (22.6 μC/cm^2) and large hysteresis is observed in pure NN (Fig. 1a), being ascribed to the irreversible FE Q phase to AFE P phase transition. Replacing Nb^{5+} by Ta^{5+} at B-site results in a pinched *P*–*E* loop with reduced P_r (8.2 μC/cm^2) and lower hysteresis in 0Ag–30Ta (Fig. 1b), showing an improved but still inadequate reversibility of FE-AFE phase transition. These phenomena represent that Ta^{5+} can stabilize the AFE P feature, but its influence is still insufficient. It is worth to note that a well-defined double *P*-*E* loop with obviously reduced P_r (2.8 μC/cm^2) and hysteresis is achieved in 30Ag–30Ta by further inducing Ag^+ at A-site (Fig. 1c), revealing good reversibility between AFE P phase and FE Q phase transition. As above discussed, both Ta^{5+} and Ag^+ have positive effect on stabilizing AFE P phase, while this concept can be strengthened by the *P*–*E* loops and *I*–*E* curves for 100*x*Ag-100*y*Ta ceramics as displayed in Fig. S1, as well as the related changes of electric properties listed in Table S1. Of particular importance is that the 30Ag–30Ta exhibits improved and maximum W_{rec} of 3.3 J/cm^3, about 27 times as high as that of NN (0.12 J/cm^3), as shown in Fig. 1d. Meanwhile, the η demonstrates a great enhancement from 4.6% for NN to 42.4% for 30Ag–30Ta. Notably, the η increases gradually with the addition of either Ta^{5+} or Ag^+ due to the decrease of hysteresis, as given in Table S1. Apart from the well-defined double *P*–*E* loop, the Ta^{5+} or/and Ag^+ modification also improve the maximum electric field by increasing activation energy (E_a) (Fig. S2) and refining grain size (Fig. S3), beneficial to the improvement of W_{rec}.

To comprehensively evaluate the stability of double *P*–*E* loop and energy storage property of 30Ag–30Ta, the related dependences on electric field, temperature and frequency were measured. Fig. 1e and Fig. S4 exhibit the bipolar *P*–*E* loops under various electric fields prior to its breakdown electric field. Liner *P*–*E* loops with low P_r (< 0.7 μC/cm^2) are observed at low and medium electric fields. Double *P*–*E* loops with obviously increased P_m are obtained at electric fields above 300 kV/cm, due to the high electric field induced reversible AFE-FE phase transition. Accordingly, the W_{rec} increases successively with increasing electric field and reaches the maximum value of 3.3 J/cm^3 at 360 kV/cm. The double *P*–*E* loops of 30Ag–30Ta exhibit good stability in the temperature range from 30 °C to 160 °C, as shown in Fig. 1g and Fig. S5, which can be further confirmed by analyzing the four-current-peak *I*–*E* curves. This leads to good temperature stability for both W_{rec} and η with respective fluctuations below 10% and 17%, as demonstrated in Fig. 1h. The 30Ag–30Ta also exhibits high stability of W_{rec} and η across the frequency range of 1–200 Hz under 320 kV/cm, with respectively variation of <16% and <±4%, as shown in Figs. S6a–b. Additionally, the discharge current-time (*I*–*t*) curves under various electric fields for 30Ag–30Ta were recorded and displayed in Fig. S6c. And the discharge energy density (W_{dis}) can be calculated based on calculated based on $W_{dis} = R\int i(t)^2 dt/V_e$ [34], where V_e and R are the sample volume and total load resistance (10,260 Ω), respectively. The W_{dis} increases with increasing electric field and reaches a maximum value of 2.5 J/cm^3 under 330 kV/cm (Fig. S6d), close to the value of 2.7 J/cm^3 calculated from the *P*–*E* loop.

The reversibility of AFE-FE phase transition is critical to achieve double *P*–*E* loop in a good AFE material. To evaluate the reversible behavior between AFE P phase and the high-electric-field induced FE Q phase, first and second cycles of *P*–*E* loops were measured for the three representative ceramics, as shown in Fig. 2a–c. A slowly increasing polarization at low electric field is observed in NN (Fig. 2a), with a sudden improvement once the electric field increases to a critical value associated with the AFE to FE phase transition. However, a large P_r up to 27.6 μC/cm^2 remains when removing electric field, indicating the high-electric field induced FE phase cannot switch back to AFE phase. The typical square shaped *P*–*E* loop in the second cycle confirms a FE nature in the high electric-field-treated sample. A similar polarization change is also observed in the first positive cycle of *P*–*E* loop in 0Ag–30Ta (Fig. 2b), showing an electric field induced AFE-FE phase transition. Despite of the partial overlap in first and second cycles of *P*–*E* loops, high P_r remains after removal of electric field, indicating the induced FE phase cannot completely switch back to virgin AFE state. Particularly, well-defined double *P*–*E* loops with significantly reduced P_r and lower hysteresis are observed in both first and second cycles in 30Ag–30Ta (Fig. 2c), demonstrating a typical AFE feature with good reversibility between AFE and FE phases. The *S*–*E* curve also serves as an indicator of the reversibility of the electric field induced AFE-FE phase transition. The NN exhibits a butterfly-shaped *S*–*E* curve with large negative strain (Fig. 2d), exhibiting the characteristic of a typical ferroelectric under electric field. The addition of Ta^{5+} in NN changes the *S*–*E* curve to sprout-like shape but cannot completely eliminate the negative strain. This may be associated with the non-180° ferroelastic domain switch due to the partial reversibility of electric induced FE phase [35]. It is worth noting that sprout-shaped *S*–*E* curve with zero negative stain is achieved in 30Ag–30Ta, demonstrating a typical AFE characteristic.

Fig. 2e shows the composition dependence of piezoelectric coefficient (d_{33}) for the three representative ceramics after high electric field treatment. A high d_{33} up to 34.6 pC/N is obtained for NN, while the d_{33} values in both 0Ag–30Ta and 30Ag–30Ta ceramics are negligible. It is generally accepted that the piezoelectricity is absent in AFEs [36]. The nearly zero d_{33} value reveals the reversible AFE-FE phase transition in 0Ag–30Ta and 30Ag–30Ta

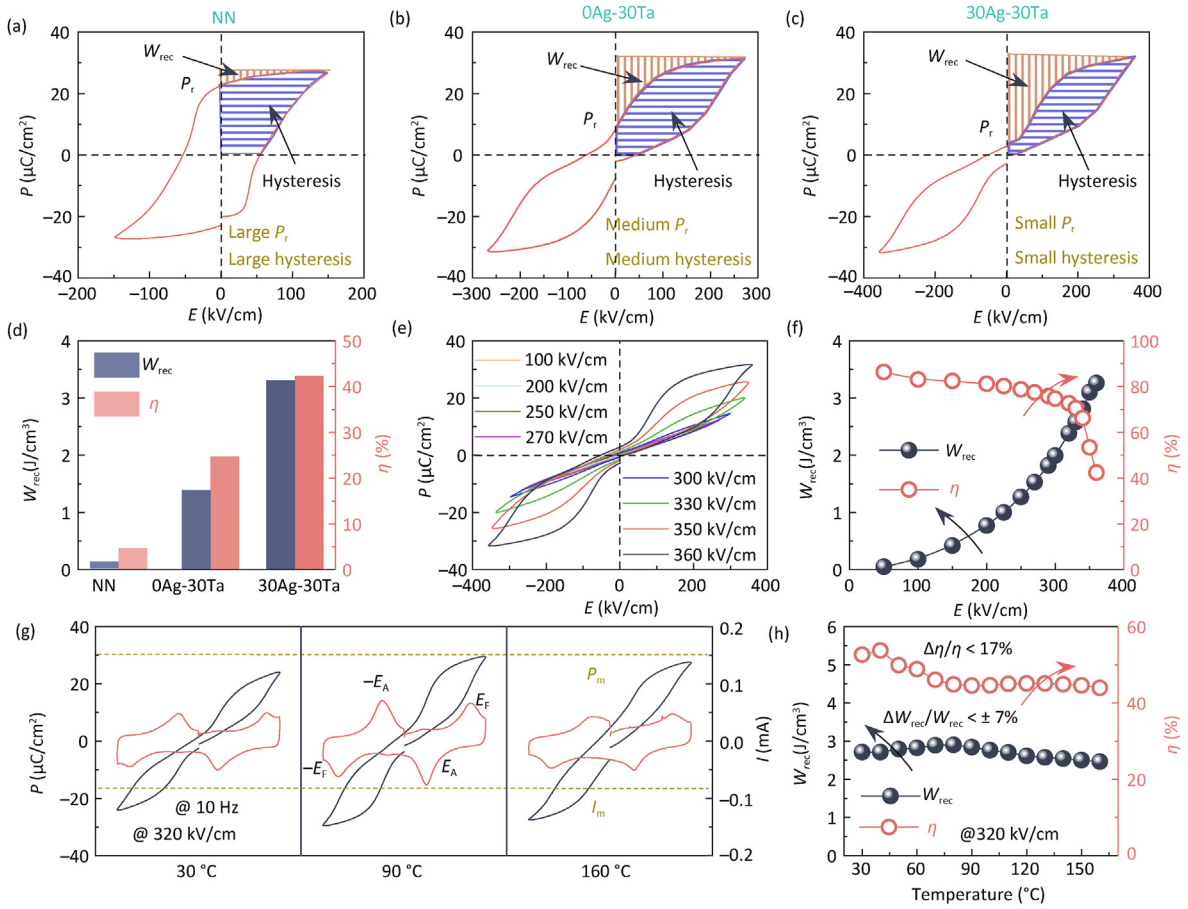

Fig. 1. *P*–*E* loops of (a) NN, (b) 0Ag–30Ta and (c) 30Ag–30Ta ceramics, and (d) corresponding W_{rec} and η. Electric field dependence of (e) *P*–*E* loops and (f) W_{rec} and η of 30Ag–30Ta. (g) and (h) are temperature dependence of *P*–*E* loops and W_{rec} and η of 30Ag–30Ta under 320 kV/cm, respectively.

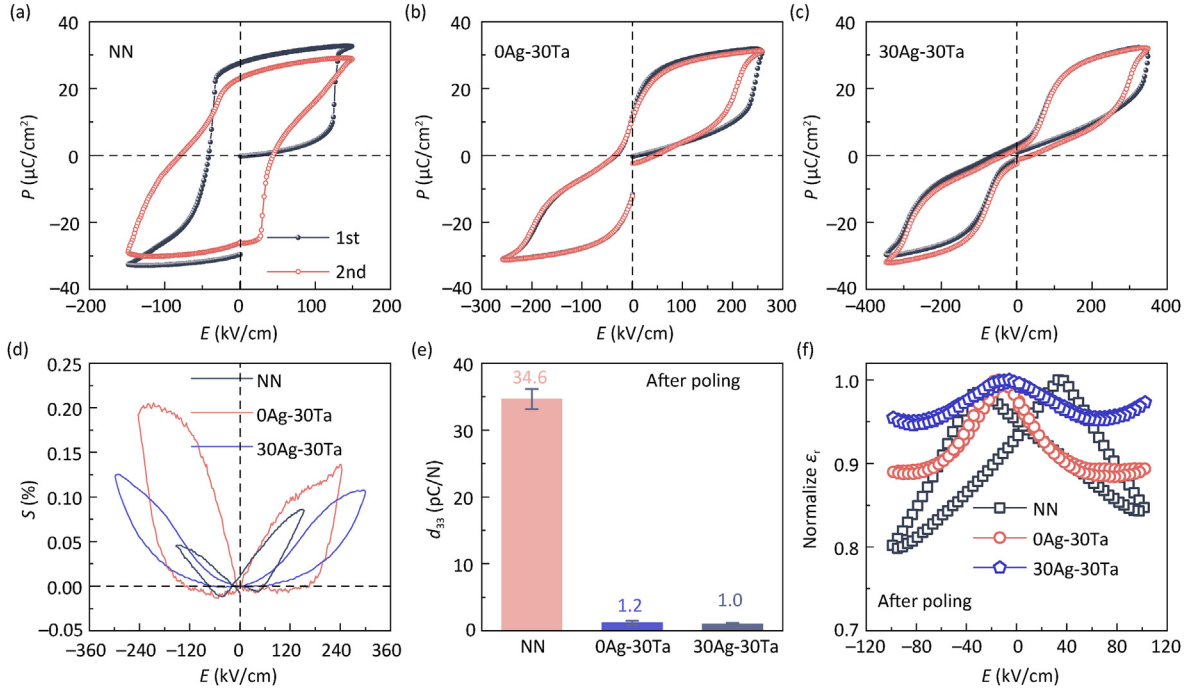

Fig. 2. First and second circles of *P*–*E* loops of (a) NN, (b) 0Ag–30Ta and (c) 30Ag–30Ta ceramics. (d) *S*–*E* curves of all compositions. (e) Piezoelectric coefficient d_{33} and (f) normalized ε_r–*E* curves at 100 kV/cm after poling of all compositions.

ceramics. The good reversibility between AFE phase and high-field-induced FE phase in Ta^{5+} or/and Ag^{+} modified NN can be further corroborated by the electric field dependence of dielectric constant, as shown in the normalized ε_r–E curves in Fig. 2f. The NN demonstrates a large reduction in ε_r with variation up to 20% under electric field, as commonly observed in FE materials. In comparison, a lower variation of ~11% is observed in 0Ag–30Ta, which further decreases to around 5% in 30Ag–30Ta. The electric field insensitive dielectric constant in 30Ag–30Ta manifests that the electric field induced FE phase is well restored to the AFE state, which accounts for the well-defined double hysteresis loop.

To investigate the reversibility between AFE and FE phases from a microscopic scale, TEM was performed on NN and 30Ag–30Ta to detect the crystal structure change in virgin and high field treated states. In NN, the special quadrupled and doubled unit cells along $[010]_p$ direction are the signatures of AFE P and FE Q phases, respectively. Hence, the superlattice diffraction of $^1/_4$ (010) type for P phase and $^1/_2$ (010) type for Q phase can be utilized to distinguish these two phases [37]. Fig. 3a presents the TEM image of virgin NN along the $[001]_p$ zone axis, in which two types of nanoregions are observed. The right region is ordered with definite nanostripes with width of ~1.6 nm and exhibits $^1/_4$ (010) type diffraction spots (Fig. 3c), giving a signature of homogeneous AFE P phase. In contrast, the ambiguous nanostripes with larger widths are observed in the left region in Fig. 3a, accompanying with diffused scattering streaking along the $[010]_p$ direction (Fig. 3d). Particularly, Fig. S7, recorded from the enlarged left region, exhibits partial nanostripes with width of ~1.6 nm for AFE P phase and typical $^1/_2$ (010) superlattice diffraction spots for FE Q phase simultaneously. Therefore, it is appropriate to conclude that the coexistence and competition between AFE P phase and FE Q phase generate this phenomenon of local incommensurate (INC) modulation [15]. After electric field treatment, only ordered and homogenous nanostripes with definite width of ~0.8 nm are observed in NN (Fig. 3b), accompanying with $^1/_2$ (010) superlattice diffraction spots (Fig. 3e), indicating a FE Q phase. This reveals that the AFE P phase transforms into FE Q phase under a specific high electric field, but the transition back to the AFE phase is prevented after removing electric field. In contrast, the nearly identical distribution of nanostripes with definite width of ~1.6 nm is observed in 30Ag–30Ta at both virgin and field treated states (Fig. 3f–g), in which the consistent $^1/_4$ (010) type diffraction spots remain at both states (Fig. 3h–i), giving a feature of AFE P phase. This implies that the induced FE Q phase cannot be maintained once the electric field is removed, which will reversibly switch back to AFE P phase. It should be noted that the measured width of nanostrip is ~1.6 nm in AFE P phase and ~0.8 nm in FE Q phase, being in consistent with the lattice parameter [38], where the difference originates from the two types of modulations.

Due to the different electromechanical coupling phenomena between AFE and FE phases, the PFM amplitude images at virgin and high electric field treated states were measured for NN and 30Ag–30Ta ceramics to further evaluate the reversibility between these two phases. A weak piezoelectric response is observed in the major regions of virgin NN accompanied by some regions of strong response, as shown in Fig. 4a. The weak response (close to zero) is the typical characteristic of AFE P phase, while the strong response is ascribed to the coexistence of FE Q phase. After high electric field treated, the NN exhibits an ordering polar and strong piezoelectric response over the entire region, as give in Fig. 4b, which are induced by the preserved FE Q phase after withdrawing electric field. Certainly, there is some variation in the response of poled NN, associating with the residual AFE P phase and/or the effect of topography [39,40]. Particularly, the PFM amplitude statistic results present almost 5 times enhancements after poled when comparing to the virgin state (Fig. 4c), further reflects the irreversible electric field induced AFE-FE phase transition. On the contrary, both virgin and poled 30Ag–30Ta samples show homogeneous and very weak piezoelectric response (Fig. 4d–e), which exhibit almost identical PFM amplitude statistic results (Fig. 4f), representing nearly uniform domain structure and consistent AFE P phase in two different conditions.

To dynamically study the electric-field induced AFE-FE phase transition, in-situ Raman spectra were conducted under various electric fields for NN and 30Ag–30Ta ceramics. We firstly measured the Raman spectra on multiple grains of virgin NN and 30Ag–30Ta ceramics before performing in-situ electric field measurement. Notably, the wavenumbers locating around < 100, ~560 cm^{-1} and ~870 cm^{-1} are employed to distinguish the AFE P and FE Q phases [41,42]. Two types of Raman spectra are detected in NN (Fig. 5a),

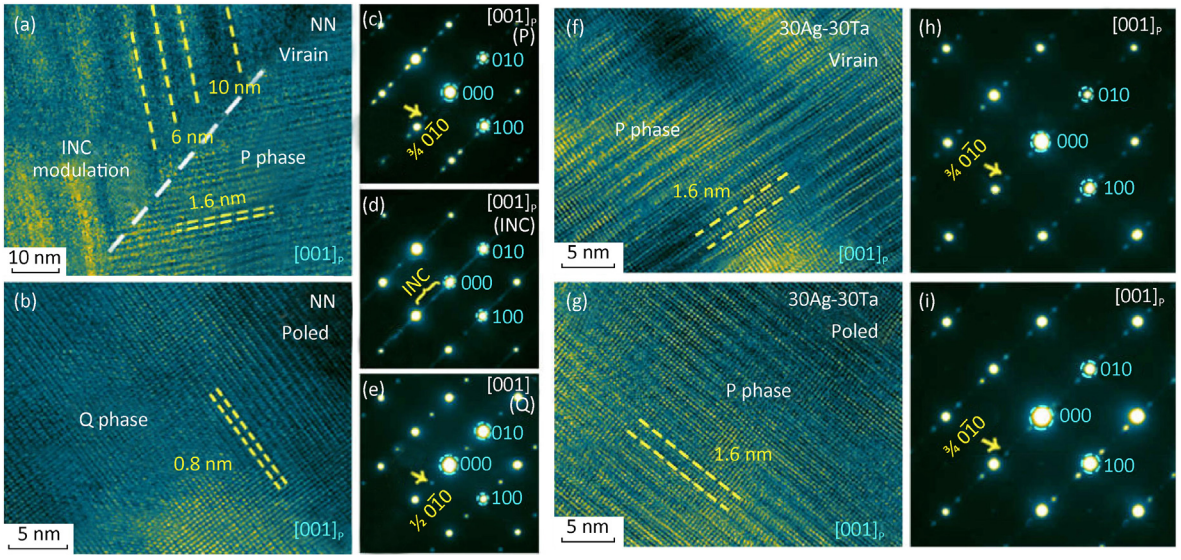

Fig. 3. TEM images of (a) virgin and (b) poled NN, (f) virgin and (g) poled 30Ag–30Ta ceramics taken from the $[001]_p$ zone axis. SAED patterns of (c), (d) virgin NN and (e) poled NN, (h) virgin and (j) poled 30Ag–30Ta ceramics taken from the $[001]_p$ zone axis.

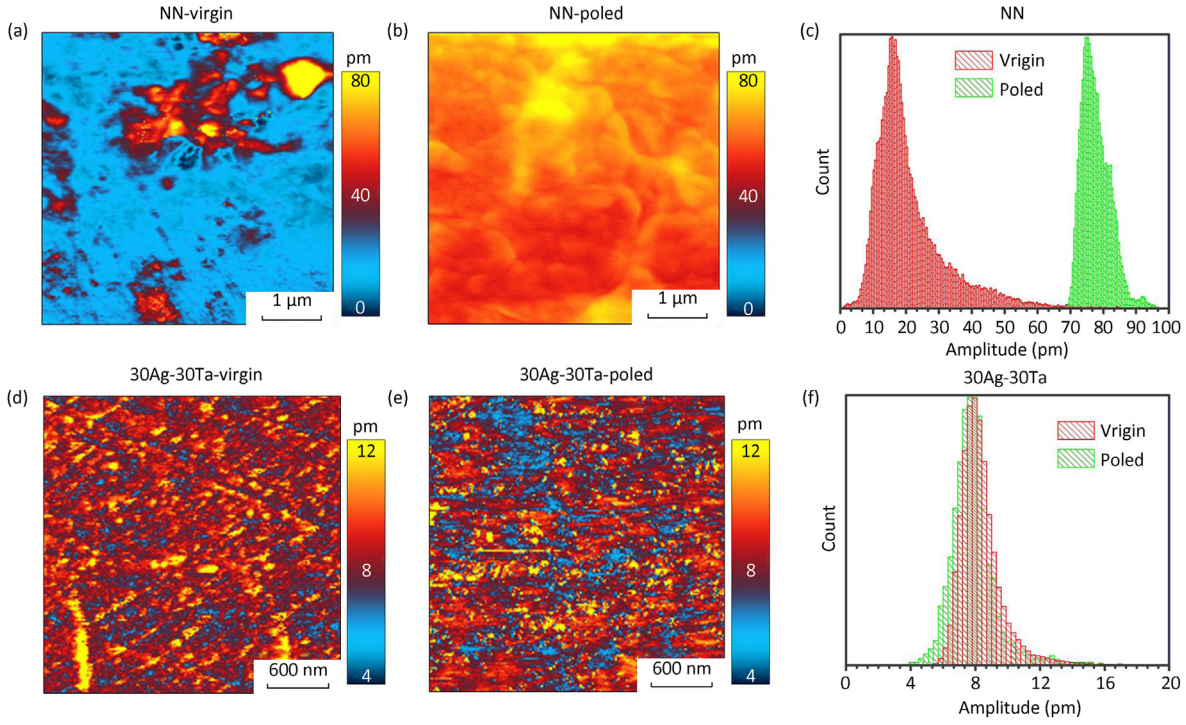

Fig. 4. PFM amplitude images of (a) virgin and (b) poled NN, (d) poled and (f) poled 30Ag–30Ta. The amplitude statistics at two states of (c) NN and (f) 30Ag–30Ta ceramics.

indicating the coexistence of AFE P and FE Q phases, in agreement with previous studies [42,43]. In comparison, only one type of Raman spectra corresponding to AFE P phase can be observed in 30Ag–30Ta, as shown in Fig. 5b. To study the reversibility of AFE and field-induced FE phase in NN, the grain with AFE P phase was chosen to measure the in-situ Raman spectra, as given in Fig. 5c. Under low electric field, the Raman spectra manifest an AFE P phase and remain unchanged. A high electric field over 70 kV/cm gradually changes the Raman spectra to FE Q phase, with the transition completing at around 120 kV/cm. It should be noted that the

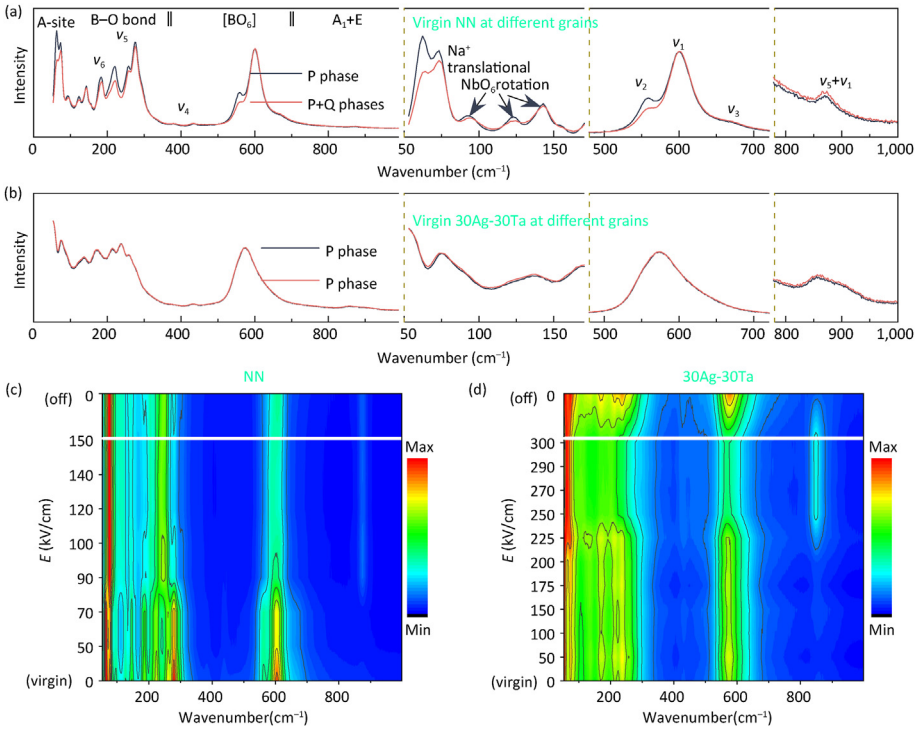

Fig. 5. Raman spectra of (a) NN and (b) 30Ag–30Ta ceramics at virgin state on different grains. Raman spectra with electric field increasing and turning off at maximum of (c) NN and (d) 30Ag–30Ta ceramics.

induced FE Q phase remains after removing high electric field, as the Raman spectra keep almost the same when the electric field is turned on and off at 150 kV/cm. A high-electric-field-induced AFE P to FE Q phase transition can also be clearly observed when the applied electric field exceeds 225 kV/cm for 30Ag–30Ta, as manifested by the obvious change in Raman spectra in Fig. 5d. It is interesting that the high-electric-field induced FE Q phase can transition back to AFE P phase after removing the electric field at 300 kV/cm, which is evidenced that the Raman spectra reverse to the shape similar to the virgin state. These finding further confirm the good reversibility between AFE P phase and the induced FE Q phase in 30Ag–30Ta.

The improved reversibility of AFE-FE phase transition from NN to 30Ag–30Ta should be closely associated with its crystal structures. To gain the underlying mechanism, the dielectric spectra, powder XRD patterns and SXRD profiles were measured. Fig. 6a and Fig. S8 present the dielectric constant and loss with increasing temperature for the three representative compositions. Two obvious dielectric anomalies are observed for NN, assigned to be INC modulation to AFE P phase (~130 °C) and AFE P to AFE R phase (~370 °C) transitions, in consistence with the previous report [15]. The addition of Ta^{5+} has little effect on the shape of dielectric spectrum, but shifts the phase transition temperatures to lower temperature. It is interesting that, in addition to the two dielectric anomalies, an abnormal broad hump locating in the temperature range of 200–300 °C comes to across in 30Ag–30Ta ceramics, as shown in Fig. 6a. To determine the phase structure evolution with temperature for 30Ag–30Ta, *in-situ* XRD at different temperatures were measured, as given in Fig. 6b. The split $(200)_C$ peak with the intensity ratio of $I_{202}/I_{080} \approx 2{:}1$ and the two apparent superlattice peaks of $\{1\frac{3}{4}1\}$ and $\{1\frac{3}{4}2\}$ showcase the AFE orthorhombic P phase structure below 200 °C. The split $(200)_C$ peaks merge into one peak as the temperature rises to 200–325 °C, accompanying with the weakening of $\{1\frac{3}{4}1\}$ peak and the disappearance of $\{1\frac{3}{4}2\}$ peak, which may indicate a gradual phase transition from P phase to R phase. At 400 °C, no superlattice and split peak can be observed, demonstrating a typical feature of paraelectric phase. To verify this, all patterns are Rietveld refined based on P, R and S (*Pbnm* space group) phases respectively using GSAS software [44], as given in Fig. S9. The good reliability factors confirm the validity of the space group adopted. The phase structure and refinement results are presented in Table S2. It is evident that the AFE R phase initially appears at 200 °C and becomes a sole phase at 325 °C. That is to say, the abnormal dielectric hump from 200 °C to 325 °C originates from the coexistence of P and R phases for 30Ag–30Ta ceramics.

The SXRD is also measured to reveal the origin of reversible AFE-FE phase transition in Ag^{+} and Ta^{5+} modified NN ceramics. Fig. 6cc' shows the Rietveld refinement plots of SXRD based on P or/and Q phases for NN, 0Ag–30Ta and 30Ag–30Ta ceramics. The Rietveld results are listed in Table S3. A majority of AFE P phase (73.7%) with minor FE Q phase (26.3%) is determined for NN, further illustrating the coexistence of AFE P and FE Q phases. On the contrary, only AFE P phase can be determined for both 0Ag–30Ta and 30Ag–30Ta. Thereafter, based on the atomic positions, the $[BO_6]$ octahedral tilting angles and cation displacements in AFE P phase can be

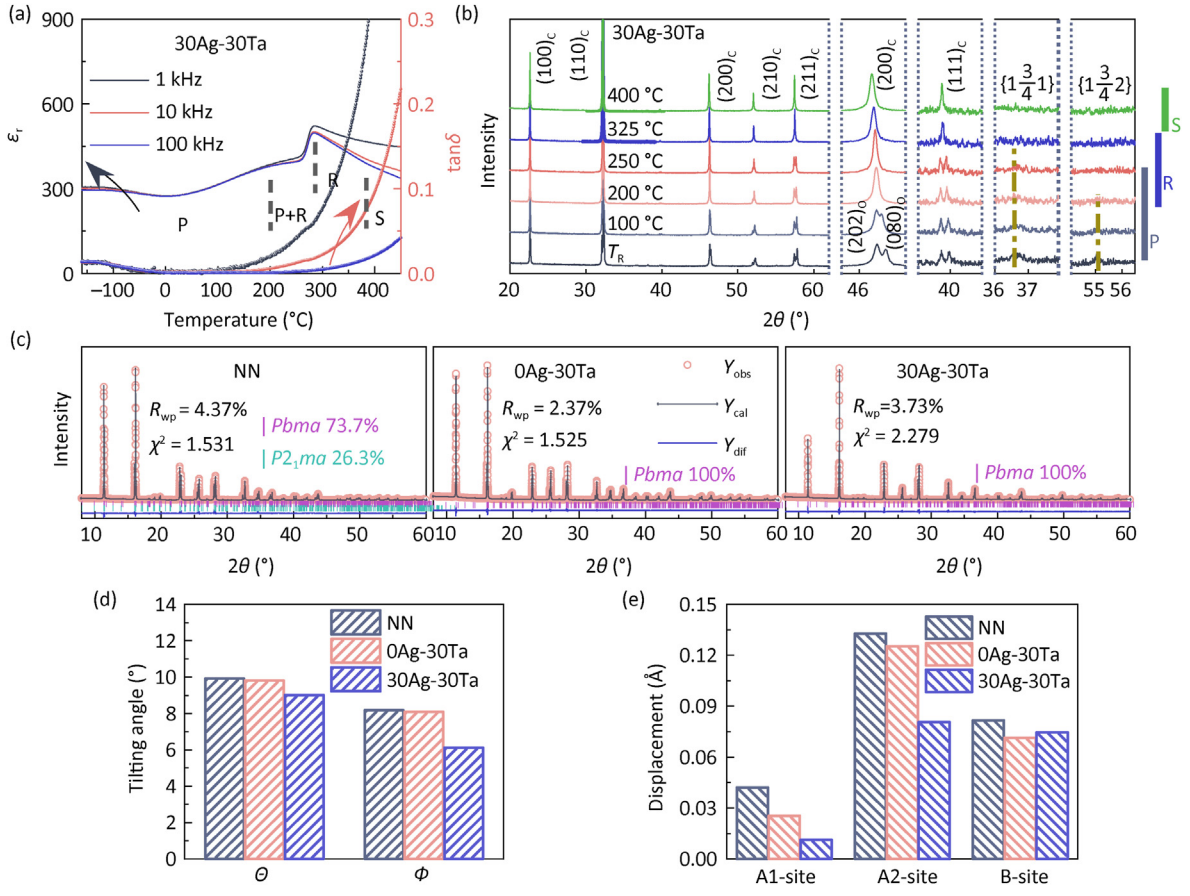

Fig. 6. (a) Temperature dependence of dielectric permittivity and loss, (b) XRD patterns with four enlarge angles around 40.0°, 46.5°, 36.7° and 55.2° for 30Ag–30Ta ceramic. (c) Rietveld refinement plots of SXRD for NN, 0Ag–30Ta and 30Ag–30Ta. (d) *a* and *b* axes tilting angles and (e) A1, A2 and B-site cation displacements of virgin P phase recorded from Rietveld refinement results of SXRD profile.

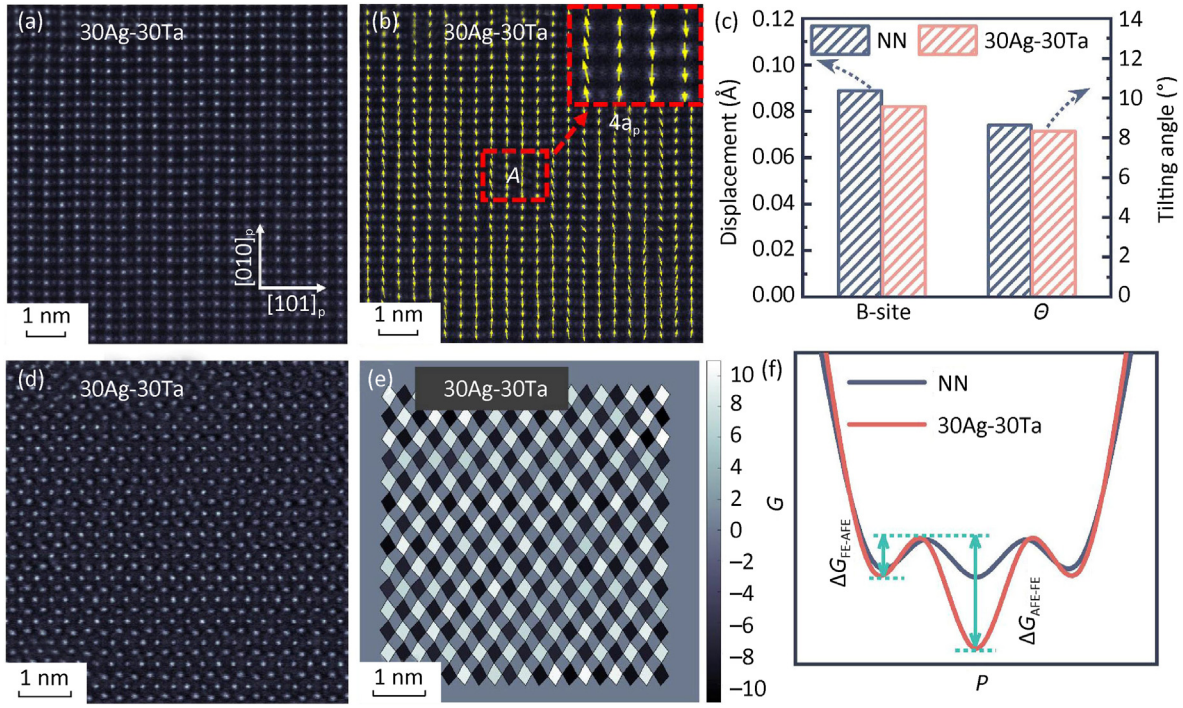

Fig. 7. Polarization field mapping of 30Ag–30Ta ceramic. (a) ADF image, (b) B-site displacement map, the right up corner shows the magnified map of region A where the yellow arrows represent the displacement vectors. (d) Bright field image, and (e) map of the antiphase oxygen octahedral tilt. (c) B-site displacements and oxygen octahedral tilting angles and (f) Schematic diagram of polarization order parameter dependence of free energy *G* of NN and 30Ag–30Ta ceramics.

determined, as depicted in Fig. 6d–e. The schematics of [BO_6] octahedral tilting angles Θ about *a* axis and Φ about *b* axis, as well as displacements of A1, A2 and B-site cations are similar to our previous work [32]. The [BO_6] octahedral tilting angles Θ and Φ decrease continuously after Ta^{5+} and Ag^{+} modifications, which respectively reach the minimum value of 9.02° and 6.22° for 30Ag–30Ta. This may be originated from the synergistic effect of the smaller size of [TaO_6] octahedra and the stronger covalent bond characteristic of Ag–O bond. To be detailed, the R_{Ta-O} (1.96 Å) is shorter than R_{Nb-O} (1.99 Å), while Ag possesses larger electronegativity (1.93) compare to Na (0.93) [45,46]. Consequently, the displacements of A1 and A2-site shift down drastically from 0.0421 Å and 0.1327 Å for NN to 0.0113 Å and 0.0806 Å for 30Ag–30Ta, respectively. Meanwhile, the B-site displacements of both 0Ag–30Ta (0.0648 Å) and 30Ag–30Ta (0.0746 Å) also exhibit obvious decrease in comparison with that of NN (0.0817 Å), indicating that the B-site ions of 0Ag–30Ta and 30Ag–30Ta are less sensitivity to electric field, in consistence with the lower polarizability of Ta^{5+} (2.82 $Å^3$) compared to Nb^{5+} (3.10 $Å^3$) [47,48]. The reduced octahedral tilting angles and cation displacements contribute to the high stability of AFE P phase and good reversibility of AFE-FE phase transition for the Ta^{5+} and Ag^{+} modified NN.

To gain insight into the microscopic mechanism, ADF STEM along $[10\,\bar{1}]_p$ zone axis was conducted to map the polarization field of 30Ag–30Ta, as shown in Fig. 7. Because of the Z-contrast is strongly depends on the atomic mass, only the positions of the B-site ions can be mapped, as shown in Fig. 7a. Herein, the phase lock-in analysis was applied to precisely map the periodic lattice displacement [49,50]. The collective atoms are mainly displaced along $[010]_p$ direction, forming a transverse displacement modulation wave with a wavelength of $4a_p$, which well reflects the antiferroelectricity, as shown in Fig. 7b. More importantly, the 30Ag–30Ta shows a reduced B-site displacement of ~0.082 Å in comparison with that of NN (~0.089 Å) reported in previous work [32], as given in Fig. 7c. This unambiguously demonstrates a suppression of the ferroelectric ordering. Fig. 7d–e shows the bright field image and map of the antiphase oxygen octahedral tilt, from which the oxygen octahedral tilting angle Θ is calculated. It should be noted that the black and white diamonds represent opposite tilting directions, and the contrast of color indicates the value of Θ. Notably, the Θ is determined to be ~8.33°, which is also smaller than that of NN (~8.62°) [32], as shown in Fig. 7c. These results are in good agreement with the SXRD analysis, which further confirm a more stable antiferroelectric state in 30Ag–30Ta.

From the viewpoint of free energy profile, based on our experimental results, the different reversibility of AFE to FE phase transition in NN and 30Ag–30Ta ceramics can be explained using the Ginzburg-Landau-Devonshire (GLD) phenomenology [51]. The small energy barrier for AFE-to-FE (ΔG_{AFE-FE}) and FE-to-AFE (ΔG_{FE-AFE}) phase transition should account for the low critical phase transition electric field in NN, as schematically illustrated in Fig. 7f. Particularly, the small difference between ΔG_{AFE-FE} and ΔG_{FE-AFE} of NN contributes to its irreversible AFE-FE phase transition. The co-doping of Ag^{+} and Ta^{5+} in NN decreases cation displacements and octahedral tilting angles, which indicates an increase of lattice compression stress and AFE distortion, enlarging the energy barrier difference between ΔG_{AFE-FE} and ΔG_{FE-AFE} [52,53]. In this scenario, the electric-field induced FE Q phase falls back to AFE P phase more easily. As a result, good reversibility from FE Q to AFE P phase transition is achieved in 30Ag–30Ta, accounting for the well-defined *P–E* loop and significantly improved energy storage density.

4. Conclusion

In this work, the Ag^{+} and Ta^{5+} modified NN ceramics were designed and fabricated *via* a conventional solid-state reaction method. The well-defined double hysteresis loop was achieved in

30Ag–30Ta by stabilizing its AFE P phase, exhibiting improved W_{rec} of 3.3 J/cm^3 and good η of 42.4% with good thermal and frequency stabilities. In contrast to the coexistence of AFE P and FE Q phases at RT in NN, only the AFE P phase was observed in 30Ag–30Ta. The SXRD and STEM results revealed that the decreased cation displacements and octahedral tilting angles were the underlying mechanism that accounted for the double *P*–*E* loop and significantly improved energy storage density. This work demonstrates the possibility of stabilizing the AFE P phase, and provides a good paradigm for realizing double hysteresis loop and achieving high energy storage density in $NaNbO_3$-based ceramics.

Declaration of competing interest

The authors declare that they have no known competing financial interests or personal relationships that could have appeared to influence the work reported in this paper.

Acknowledgements

This work was financially supported by the National Natural Science Foundation of China (Grant No. 52072080 and 52388201) and Guangxi Natural Science Fund for Distinguished Young Scholars (Grant No. 2022GXNSFFA035034). Y.Z. acknowledges the support of the Research Grants Council of Hong Kong (Grant No. C5029-18E). J.L. acknowledges the support of Tsinghua-Foshan Innovation Special Fund (TFISF) under Grant No. 2020THFS0113. Y.L. acknowledges the support of Hunan Provincial Natural Science Foundation of China (No. 2021JJ10006).

Appendix A. Supplementary data

Supplementary data to this article can be found online at https://doi.org/10.1016/j.jmat.2023.11.003.

References

[1] Tang TX, Yang WF, Shen ZH, Wang J, Guo MF, Xiao Y, et al. Compressible polymer composites with enhanced dielectric temperature stability. Adv Mater 2023;35(16):2209958.
[2] Zhang GZ, Zhang SJ, Wang Q. Dielectric materials for electrical energy storage. J Materiomics 2022;8(6):1287–9.
[3] Yang LT, Kong X, Li F, Hao H, Cheng ZX, Liu HX, et al. Perovskite lead-free dielectrics for energy storage applications. Prog Mater Sci 2019;102:72–108.
[4] Pan H, Li F, Liu Y, Zhang QH, Wang M, Lan S, et al. Ultrahigh–energy density lead-free dielectric films *via* polymorphic nanodomain design. Science 2019;365(6453):578–82.
[5] Wu SY, Fu B, Zhang JJ, Du HW, Zong Q, Wang JY, et al. Superb energy storage capability for $NaNbO_3$-based ceramics featuring labyrinthine submicrodomains with clustered lattice distortions. Small 2023;19(45):2303915.
[6] Shkuratov SI, Lynch CS. A review of ferroelectric materials for high power devices. J Materiomics 2022;8(4):739–52.
[7] Zhao PY, Li LT, Wang XH. $BaTiO_3$-$NaNbO_3$ energy storage ceramics with an ultrafast charge-discharge rate and temperature-stable power density. Microstructures 2023;3(1):2023002.
[8] Che ZY, Ma L, Luo GG, Xu C, Cen ZY, Feng Q, et al. Phase structure and defect engineering in $(Bi_{0.5}Na_{0.5})TiO_3$-based relaxor antiferroelectrics toward excellent energy storage performance. Nano Energy 2022;100:107484.
[9] Han K, Luo NN, Mao SF, Zhuo FP, Liu LJ, Peng BL, et al. Ultrahigh energy-storage density in A-/B-site co-doped $AgNbO_3$ lead-free antiferroelectric ceramics: insight into the origin of antiferroelectricity. J Mater Chem A 2019;7(46):26293–301.
[10] He LQ, Yang Y, Liu C, Ji YC, Lou XJ, Zhang LX, et al. Superior energy storage properties with thermal stability in lead-free ceramics by constructing an antiferroelectric/relaxor-antiferroelectric crossover. Acta Mater 2023;249:118826.
[11] Yang D, Zhang YY, Wang XP, Li Q, Li JF. Antiferroelectricity of $NaNbO_3$: single-crystal experimental study and first-principles calculation. J Am Ceram Soc 2022;105(9):5555–61.
[12] Vousden P. The structure of ferroelectric sodium niobate at room temperature. Acta Crystallogr 1951;4(6):545–51.
[13] Zhang MH, Fulanovic L, Zhao CH, Koruza J. Review on field-induced phase transitions in lead-free $NaNbO_3$-based antiferroelectric perovskite oxides for energy storage. J Materiomics 2023;9(1):1–18.
[14] Zhang MH, Fulanović L, Egert S, Ding H, Groszewicz PB, Kleebe H-J, et al. Electric-field-induced antiferroelectric to ferroelectric phase transition in polycrystalline $NaNbO_3$. Acta Mater 2020;200:127–35.
[15] Guo HZ, Shimizu H, Randall CA. Direct evidence of an incommensurate phase in $NaNbO_3$ and its implication in $NaNbO_3$-based lead-free antiferroelectrics. Appl Phys Lett 2015;107(11):112904.
[16] Zhang MH, Hadaeghi N, Egert S, Ding H, Zhang HB, Groszewicz PB, et al. Design of lead-free antiferroelectric $(1-x)NaNbO_3$–$xSrSnO_3$ compositions guided by first-principles calculations. Chem Mater 2021;33(1):266–74.
[17] Liu ZY, Lu JS, Mao YQ, Ren PR, Fan HQ. Energy storage properties of $NaNbO_3$-$CaZrO_3$ ceramics with coexistence of ferroelectric and antiferroelectric phases. J Eur Ceram Soc 2018;38(15):4939–45.
[18] Zhang MH, Ding H, Egert S, Zhao CH, Villa L, Fulanović L, et al. Tailoring high-energy storage $NaNbO_3$-based materials from antiferroelectric to relaxor states. Nat Commun 2023;14(1):1525.
[19] Qi H, Zuo RZ, Xie AW, Tian A, Fu J, Zhang Y, et al. Ultrahigh energy-storage density in $NaNbO_3$-based lead-free relaxor antiferroelectric ceramics with nanoscale domains. Adv Funct Mater 2019;29(35):1903877.
[20] Chen ZG, Mao SF, Ma L, Luo GG, Feng Q, Cen ZY, et al. Phase engineering in $NaNbO_3$ antiferroelectrics for high energy storage density. J Materiomics 2022;8(4):753–62.
[21] Jiang J, Li XJ, Li L, Zhang J, Wang J, Zhu HG, et al. Novel lead-free $NaNbO_3$-based relaxor antiferroelectric ceramics with ultrahigh energy storage density and high efficiency. J Materiomics 2022;8(2):295–301.
[22] Wei XK, Jia CL, Du HC, Roleder K, Mayer J, Dunin-Borkowski RE. An unconventional transient phase with cycloidal order of polarization in energy-storage antiferroelectric $PbZrO_3$. Adv Mater 2020;32(9):1907208.
[23] Li DX, Guo QH, Cao MH, Yao ZH, Liu HX, Hao H. The influence of A/B-sites doping on antiferroelectricity of PZO energy storage films. Microstructures 2023;3(1):2023007.
[24] Gao LS, Guo HZ, Zhang SJ, Randall CA. Stabilized antiferroelectricity in $xBiScO_3$-$(1-x)NaNbO_3$ lead-free ceramics with established double hysteresis loops. Appl Phys Lett 2018;112(9):092905.
[25] Ye JM, Wang GS, Chen XF, Cao F, Dong XL. Enhanced antiferroelectricity and double hysteresis loop observed in lead-free $(1-x)NaNbO_3$-$xCaSnO_3$ ceramics. Appl Phys Lett 2019;114(12):122901.
[26] Shimizu H, Guo HZ, Reyes-Lillo SE, Mizuno Y, Rabe KM, Randall CA. Lead-free antiferroelectric: $xCaZrO_3$-$(1-x)NaNbO_3$ system ($0 \le x \le 0.10$). Dalton Trans 2015;44(23):10763–72.
[27] Qi H, Li WC, Wang L, Chen LQ, Liu HT, Deng SQ, et al. Large (anti)ferrodistortive $NaNbO_3$-based lead-free relaxors: polar nanoregions embedded in ordered oxygen octahedral tilt matrix. Mater Today 2022;60:91–7.
[28] Xie AW, Fu J, Zuo RZ, Zhou C, Qiao ZL, Li TY, et al. $NaNbO_3$-$CaTiO_3$ lead-free relaxor antiferroelectric ceramics featuring giant energy density, high energy efficiency and power density. Chem Eng J 2022;429:132534.
[29] King G, Woodward PM. Cation ordering in perovskites. J Mater Chem 2010;20(28):5785–96.
[30] Lu T, Studer AJ, Yu DH, Withers RL, Feng YJ, Chen H, et al. Critical role of the coupling between the octahedral rotation and A-site ionic displacements in $PbZrO_3$-based antiferroelectric materials investigated by in situ neutron diffraction. Phys Rev B 2017;96(21):214108.
[31] Saito T, Chen WT, Mizumaki M, Attfield JP, Shimakawa Y. Magnetic coupling between A' and B sites in the A-site-ordered perovskite $BiCu_3Mn_4O_{12}$. Phys Rev B 2010;82(2):024426.
[32] Luo NN, Ma L, Luo GG, Xu C, Rao LX, Chen ZG, et al. Well-defined double hysteresis loop in $NaNbO_3$ antiferroelectrics. Nat Commun 2023;14(1):1776.
[33] Liu H, Zhou ZY, Qiu Y, Gao BT, Sun SD, Lin K, et al. An intriguing intermediate state as a bridge between antiferroelectric and ferroelectric perovskites. Mater Horiz 2020;7(7):1912–8.
[34] Ma L, Che ZY, Xu C, Cen ZY, Feng Q, Chen XY, et al. High energy storage density and efficiency in $AgNbO_3$ based relaxor antiferroelectrics with reduced silver content. J Eur Ceram Soc 2023;43(8):3228–35.
[35] Feng W, Luo BC, Bian SS, Tian E, Zhang ZL, Kursumovic A, et al. Heterostrain-enabled ultrahigh electrostrain in lead-free piezoelectric. Nat Commun 2022;13(1):5086.
[36] Albino M, Heijboer P, Porcher F, Decourt R, Veber P, Maglione M, et al. Metastable ferroelectric phase and crossover in the $Ba_2NdFeNb_4$–xTa_xO_{15} TTB solid solution. J Mater Chem C 2018;6(6):1521–34.
[37] Chen J, Feng D. TEM study of phases and domains in $NaNbO_3$ at room temperature. Phys Status Solidi 1988;109(1):171–85.
[38] Chen M, Pu YP, Ding H, Zhang L, Xu N, Kleebe HJ, et al. Phase identification and structural evolution in BMT modified NN anti-ferroelectric ceramics. J Eur Ceram Soc 2022;42(14):6504–11.
[39] Cai RG, Antohe VA, Nysten B, Piraux L, Jonas AM. Thermally induced flexo-type effects in nanopatterned multiferroic layers. Adv Funct Mater 2020;30(14):1910371.
[40] Qu N, Du HL, Hao XH. A new strategy to realize high comprehensive energy storage properties in lead-free bulk ceramics. J Mater Chem C 2019;7(26):7993–8002.
[41] Lima RJC, Freire PTC, Sasaki JM, Ayala AP, Melo FEA, Mendes Filho J, et al. Temperature-dependent Raman scattering studies in $NaNbO_3$ ceramics. J Raman Spectrosc 2002;33(8):669–74.
[42] Shakhovoy RA, Raevskaya SI, Shakhovaya LA, Suzdalev DV, Raevski IP, Yuzyuk YI, et al. Ferroelectric Q and antiferroelectric P phases' coexistence and

local phase transitions in oxygen-deficient $NaNbO_3$ single crystal: micro-Raman, dielectric and dilatometric studies. J Raman Spectrosc 2012;43(8):1141–5.
[43] Li W, Xia X, Zeng JT, Zheng LY, Li GR. Significant differences in $NaNbO_3$ ceramics fabricated using Nb_2O_5 precursors with various crystal structures. Ceram Int 2020;46(3):3759–66.
[44] Toby B. EXPGUI, a graphical user interface for GSAS. J Appl Crystallogr 2001;34(2):210–3.
[45] Levin I, Woicik JC, Llobet A, Tucker MG, Krayzman V, Pokorny J, et al. Displacive ordering transitions in perovskite-like $AgNb_{1/2}Ta_{1/2}O_3$. Chem Mater 2010;22(17):4987–95.
[46] WebElements. https://www.webelements.com/periodicity/electronegativity/. [Accessed 3 November 2023].
[47] Zhao L, Liu Q, Gao J, Zhang SJ, Li JF. Lead-free antiferroelectric silver niobate tantalate with high energy storage performance. Adv Mater 2017;29(31):1701824.
[48] Shannon RD, Fischer RX. Empirical electronic polarizabilities in oxides, hydroxides, oxyfluorides, and oxychlorides. Phys Rev B 2006;73(23):235111.
[49] Savitzky BH, El Baggari I, Admasu AS, Kim J, Cheong S-W, Hovden R, et al. Bending and breaking of stripes in a charge ordered manganite. Nat Commun 2017;8(1):1883.
[50] Xu C, Chen YC, Cai XB, Meingast A, Guo XY, Wang FK, et al. Two-dimensional antiferroelectricity in nanostripe-ordered In_2Se_3. Phys Rev Lett 2020;125(4):047601.
[51] Chen M, Pu YP, Zhang L, Shi Y, Zhuo FP, Zhang QW, et al. Realizing room temperature double hysteresis loops in antiferroelectric $NaNbO_3$ based ceramics. Ceram Int 2021;47(15):21303–9.
[52] Zhang TD, Zhao Y, Li WL, Fei WD. High energy storage density at low electric field of ABO_3 antiferroelectric films with ionic pair doping. Energy Storage Mater 2019;18:238–45.
[53] Tolédano P, Guennou M. Theory of antiferroelectric phase transitions. Phys Rev B 2016;94(1):014107.

Nengneng Luo is a professor in School of Resources, Environment and Materials, Guangxi University. He received his Ph.D. degree in Chemistry from Tsinghua University in 2015. He studied at the Pennsylvania State University as a joint-training Ph.D. student from 2013 to 2014. His research activity is focused on designing novel high-performance lead-free (anti)ferroelectric materials and their application for energy storage/piezoelectric sensor, and finding the correlations between microstructure (such as crystal structure, domain wall, defect, etc.) and physical performance.

Li Ma is a Ph.D. candidate under the supervision of Prof. Nengneng Luo in the school of chemistry and chemical engineering at Guangxi University, Nanning, China. His primary research interests include the phase transition and energy storage property of silver niobate and sodium niobate-based antiferroelectric ceramic and the development of new lead-free antiferroelectric materials.